applied sciences

MDPI

Article

Development and Initial Characterisation of a Localised Elastin Degradation Ex Vivo Porcine Aortic Aneurysm Model

Matthew Laffey [1,2], Brooke Tornifoglio [1,2,*] and Caitríona Lally [1,2,3,*]

[1] Trinity Centre for Biomedical Engineering, Trinity Biomedical Sciences Institute, Trinity College Dublin, D02 R590 Dublin, Ireland; laffeym@tcd.ie
[2] Department of Mechanical, Manufacturing and Biomedical Engineering, School of Engineering, Trinity College Dublin, D02 R590 Dublin, Ireland
[3] Advanced Materials and Bioengineering Research Centre (AMBER), Royal College of Surgeons in Ireland and Trinity College Dublin, D02 W05 Dublin, Ireland
* Correspondence: btornifo@tcd.ie (B.T.); lallyca@tcd.ie (C.L.)

Abstract: Aortic aneurysms (AA) occur in 4.8% of people causing 150,000 deaths annually. While endovascular aneurysm repairs reduce surgical morbidity, device-related failures (leak/displacement) are frequent highlighting the need for test models that better represent the mural geometry and compliance changes in human AAs. We aimed to develop and characterise an ex vivo porcine aortic model of AA. The optimal duration of tissue elastase exposure to emulate AA changes in elastin microstructure and content was determined using porcine aortic rings. Elastase-induced changes were quantified morphologically, and mechanical properties assessed via ring tensile testing. Subsequent experiments tested the potential for localised elastase treatment in a 1 cm segment of porcine aorta using a specially designed 3D printed rig. The effect on pressure-diameter behaviour was investigated via inflation-extension testing. Elastase treatment produced time dependent decreases in elastin, resulting in an increased tensile modulus and circumferential length in the ring samples in the final phase of the J-shaped tissue stress-strain curves. In whole aortic segments, localised elastase-induced luminal degradation was successfully limited to a central region. The degree of elastin degradation achieved was sufficient to cause localised dilation with respect to controls under physiological pressures. Localised elastin degradation in porcine aortic segments is feasible and emulates the changes seen clinically in aortic aneurysms.

Keywords: aortic aneurysm; ex vivo; aortic model; elastin; elastase; mechanical testing; stent-graft

check for updates

Citation: Laffey, M.; Tornifoglio, B.; Lally, C. Development and Initial Characterisation of a Localised Elastin Degradation Ex Vivo Porcine Aortic Aneurysm Model. *Appl. Sci.* **2023**, *13*, 9894. https://doi.org/10.3390/app13179894

Academic Editors: Salvatore Pasta and Miquel Aguirre

Received: 17 July 2023
Revised: 25 August 2023
Accepted: 29 August 2023
Published: 1 September 2023

Copyright: © 2023 by the authors. Licensee MDPI, Basel, Switzerland. This article is an open access article distributed under the terms and conditions of the Creative Commons Attribution (CC BY) license (https://creativecommons.org/licenses/by/4.0/).

1. Introduction

Aneurysms of the thoracic and abdominal aorta constitute a clinical disorder defined by dilation beyond 50% of their normal diameter [1]. They affect approximately 4.8% of the world's population [2] and cause over 150,000 fatalities each year [3]. Endovascular aneurysm repair using a stent graft is the preferred mode of treatment in both thoracic and abdominal aortic aneurysms (TAA, AAA, respectively) in the elective setting due to its lower short-term morbidity and mortality compared to open surgical repair [4,5]. Furthermore, endovascular techniques demonstrate promise and are becoming increasingly popular in the management of ruptured aortic aneurysms [5,6]. However, the advantages in morbidity and mortality of EVAR in the elective setting over open surgical repair are offset after 3 years due to a higher rate of post-procedural device-related complications requiring reintervention [4]. The complication rate for EVAR ranges from 16–30% with 19% of patients requiring reintervention [7]. The most common complications relate to device failure including device leakage (endoleaks) which occurs in 15–30% of endovascular AAA repairs within the first 30 days [8,9] and 4–15% of endovascular TAA repairs [10–12]; device migration or displacement which occurs in 1–2.8% of endovascular repairs of TAAs and 1–10% of endovascular repairs of abdominal aortic aneurysms at 1 year [10,11,13,14];

and device kinking and fracture [7,15].There is a need to optimise endovascular aneurysm repair devices to maintain functionality in the challenging mechanical environment present in aortic aneurysms (AA) [16–19].

An implanted stent graft must match both the dilation and recoil of the vessel wall during the cardiac cycle and withstand the haemodynamic forces imposed by flowing blood to maintain a proper seal and fixation [7]. Not only are the geometry of the aorta and the pressure-flow characteristics of the blood important, but the compliance of the vessel wall must also be taken into account [20]. The healthy arterial wall exhibits non-linear hyperelastic behaviour characterised by an increasing stiffness with increasing deformation resulting in a J-shaped stress-strain curve [21]. This behaviour is attributed to the initial recruitment of elastin fibres in conjunction with the progressive strain-dependent recruitment of stiff collagen fibres [16,22]. Destruction and degeneration of mural elastin fibres is widely believed to cause the increases in stiffness seen in AA through the resultant load being taken up by the stiffer collagen fibres [17,23,24]. As such, the mechanical environment present in AA differs from that found in healthy aortae because of both the locally dilated vessel geometry and decreased mural compliance. Optimisation of endovascular devices using in vitro benchtop models, which recapitulate these changes in geometry and compliance, offers a means to address, and ultimately reduce, the incidence of endovascular device complications secondary to mechanical failures.

In vitro models represent an invaluable tool in facilitating the refinement and optimisation of device designs prior to costly preclinical in vivo trials [25,26]. The ex vivo porcine aorta is the most utilised model based on its widespread availability and structural similarity to healthy human aortae [27–30]. However, it does not replicate the dilation nor the stiffening seen in AA [31]. While synthetic models can accurately replicate the geometric features of aneurysms, the materials used poorly replicate the compliance and rupture properties of arterial tissues [20,32–35]. Currently available tissue engineered in vitro models are more suited to studies of aneurysm pathophysiology and have not yet been manufactured on a scale suitable for endovascular device testing [36–38]. At present, there are no suitable in vitro models which accurately reproduce a physiologically relevant environment for endovascular device testing.

Enzymatic treatments represent a promising avenue to induce microstructural changes which mimic the increases in diameter and stiffness seen in AA. In a seminal study by Roach et al., human iliac arteries treated with crude trypsin for elastin degradation demonstrated a greater diameter and significantly greater stiffness under low hydrostatic pressures [16]. Following on from this, Dobrin et al. reported that elastin-depleted human iliac arteries exhibit decreased distensibility and only moderate dilation under physiological pressures; therefore, demonstrating the feasibility of this approach as a mechanical model for aneurysms [39]. In elastin-depleted strips of porcine aorta, Kratzberg et al. reported that a near aneurysmal increase in unloaded circumferential length can be achieved through application of a creep-loading protocol [40]. Furthermore, Chow et al. reported that a mild elastase treatment produces gradual changes in the biaxial stress-strain behaviour of porcine aortic strips characterised by increasing stiffness with increasing elastase incubation time [41]. The viability of this approach is further supported by the successful use of elastase treatments to produce models of aneurysms in small vessels in an ex vivo setting [42,43] and in vivo AA models in small and large animals [44,45]. Researchers have been studying the effects of elastase on a wide range of in vitro and in vivo arterial tissues since the 1950s [16]. Despite this, a large scale ex vivo model of an aneurysm, suitable for endovascular device benchtop testing, has yet to be developed.

We hypothesized that the localised application of elastase to porcine aortic segments would constitute a feasible methodology to recapitulate the critical features of the mechanical environment present within AA, specifically: increased diameter and stiffness under physiological pressures. To test this hypothesis, first the effect of elastase treatment on aortic geometry and tensile behaviour was studied in rings of porcine aorta to demonstrate proof-of-principle. Subsequently, locally elastin-depleted whole aortae were produced using a

specially designed degradation rig and the changes in pressure-diameter behaviour were measured via inflation extension testing. Together this work aimed to show the viability of a localised degradation approach to produce porcine aortae with aneurysmal geometry and compliance; therefore, making it a viable preclinical ex vivo model for endovascular device testing.

2. Materials and Methods

2.1. Tissue Preparation and Elastin Degradation

Thoracic aortae from 6-month-old healthy white pigs were obtained from a local abattoir. Loose connective tissue was debrided, and samples were cryopreserved within 3 h of sacrifice as described previously [46]. Briefly, debrided samples were placed in 50 mL falcon tubes containing tissue freezing medium consisting of RPMI medium (BioSciences, Dublin, Ireland), sucrose (Sigma-Aldrich, Burlington, VT, USA), and dimethylsulfoxide (VWR International, Radnor, PA, USA) before being cooled at a controlled rate of 1 °C/min to −80 °C in a Mr. Frosty container (Sigma-Aldrich, Burlington, VT, USA). Samples were thawed at 37 °C and rinsed with phosphate buffered saline (PBS) to remove excess cryoprotectant prior to experiments. Elastase treatment solution consisted of 1 U/mL elastase (Sigma-Aldrich, Burlington, VT, USA); 0.35 mg/mL of trypsin inhibitor (Sigma-Aldrich, Burlington, VT, USA; and Dulbecco's modified eagle medium (DMEM) (BioSciences, Dublin, Ireland). Controls were treated with DMEM alone.

Individual ring samples were enzymatically digested to inform the degradation protocols for whole aorta models. Experimental groups are provided in Table 1. For the ring testing, 2 mm wide rings were cut adjacently from descending porcine aortae and placed in PBS in a 12-well plate (N = 5 pigs, n = 5 samples). Once all rings were cut, the PBS was replaced with 2 mL of either elastase or control solution so as to cover the entire sample and well plates were placed on a shaker at 99 RPM in an oven at 37 °C for the designated incubation time. After incubation, samples were rinsed with PBS and cryopreserved as described above. All rings underwent two cryopreservation cycles.

Table 1. Experimental groups for both individual aortic rings and whole aortic segments.

Aortic Sample	Treatment	Elastase Concentration [U/mL]	Incubation Time [h]	N [Pigs]	n [Samples]
2 mm ring	Control	0	9	5	5
2 mm ring	Elastase	1	9	5	5
2 mm ring	Elastase	1	18	5	5
2 mm ring	Elastase	1	27	5	5
2 mm ring	Control	0	27	5	5
6 cm segment	Control	0	9	3	3
6 cm segment	Elastase	1	9	3	3

For whole aorta models, a customised apparatus was designed, printed (PLA), and used to localise treatment to a 1 cm intraluminal section of a 6 cm long aorta (Figure 1). The 3D printed apparatus consisted of a bath, grips and proximal and distal grip holder components as shown in Figure 1a. Treatment was localised to a 1 cm segment by creating a seal between externally applied zip ties and intra-luminally placed cylindrical hollow grips (Figure 1b,c). Parafilm was applied to both intra- and extra-luminal surfaces to minimise tissue damage associated with zip-tying and to limit enzyme perfusion through the vessel wall. Once secured, aortae were cannulated to tubing and placed in the degradation rig as shown in Figure 1d. Table 1 includes the two whole aorta treatment groups. Elastase and control solutions were prepared as described previously and perfused through the intra-luminal tubing to ensure there were no air bubbles. The outer bath was filled with pre-heated PBS at 37 °C. The whole degradation rig was then placed on a shaker at 99 RPM in an oven at 37 °C and the aorta rotated 120° every 1.5 h throughout the 9-h incubation

period. Following incubation, aortae were removed, rinsed in PBS and cryopreserved. All whole aortae underwent two cryopreservation cycles.

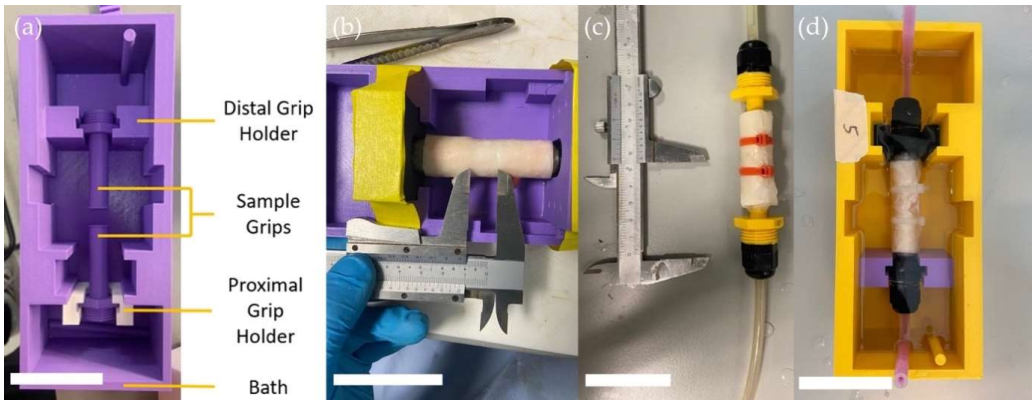

Figure 1. Developed ex vivo aortic treatment apparatus. (**a**) 3D printed apparatus, (**b**) measurement of localised 1 cm treatment region, (**c**) 'gripped' aorta for treatment, and (**d**) placement of aorta in 3D printed treatment apparatus. All scale bars are 5 cm.

2.2. Mechanical Testing

Individual ring models were assessed via ring tensile testing, whereas full aortae were assessed via inflation-extension testing.

2.2.1. Ring Tensile Testing

A materials testing device (ZwickRoell, Ulm, Germany) with a 200 N load cell was fitted with horizontally oriented pins and used to conduct tensile tests on rings of porcine aorta. Prior to testing, rings were imaged against graph paper to allow measurement of wall thickness and circumference optically using ImageJ (version 1.53r) analysis software [47]. The thickness of each ring was measured perpendicular to tangent lines constructed at the inner mural border at four equidistant locations on each sample. The circumferential length was measured as the circumference of an ellipse fit to the outer mural border for each sample. The pins used were 1 mm in diameter and all tests were performed within a PBS bath kept at a temperature of 37 °C. To begin testing, rings were loaded to hang freely from the top pin without contacting the lower pin and the force was set to zero. The test protocol involved preloading rings to 0.05 N at 10 mm/min and five preconditioning cycles to 10% strain at a rate of 60% the initial gauge length (L_0) per minute. Data was collected from the end of the fifth preconditioning cycle, when rings were stretched from 0% strain to failure at a fixed strain rate of 40% L_0/min. After failure, force-displacement and gauge length data were exported and the rings were fixed for histological analysis.

Force-displacement data was converted to Cauchy and Green-Lagrange definitions of stress and strain, respectively, using equations published by Macrae et al. [48]. First, the circumferential stretch was calculated as [48]:

$$\lambda_1 = \frac{l + \pi r_w}{l_0 + \pi r_w} \tag{1}$$

where λ is the calculated stretch factor, r_w is the pin radius, and l and l_0 represent the distance between the center of each pin in the deformed and undeformed configurations, respectively; subscript 1 denotes the circumferential axis of loading. Green strain E was calculated as [48]:

$$E_{11} = \frac{1}{2}\left(\lambda_1^2 - 1\right) \tag{2}$$

Cauchy stress was calculated on the assumptions of plane stress and incompressibility [48]:

$$\sigma_1 = \frac{F_1 \lambda_1}{2tw} \quad (3)$$

where F is the force, t the thickness and w the width. Cauchy stress and Green strain data were plotted as stress-strain curves, from which the elastic moduli were calculated over initial and final regions as described by Campbell et al. [49]. Initial and final moduli were calculated as the slope of linear regressions plotted from 0–0.05 Green strain and 0.25–0.3 MPa Cauchy stress, respectively.

2.2.2. Inflation-Extension Testing

Inflation-extension testing assessed the quasi-static pressure-diameter behaviour of whole aortic samples at 30 mmHg pressure steps from 0 mmHg to 150 mmHg using another custom designed rig, shown in Figure 2a. Sample ends were secured to cylindrical grips using zip-ties allowing insertion into the testing rig. The outer bath was filled with PBS at 37 °C and a physiologic axial strain of 1.35 [50] was imposed using an attached micrometer. Samples were flushed with PBS to remove any air bubbles prior to testing. Intraluminal hydraulic pressurisation was achieved by threading a condom through the vessel and inflating this on account of their watertight nature, negligible stiffness, and greater unstretched diameter with respect to the aortic specimens [51]. Aortic side branches were closed with sutures. Pressures were maintained at each step using a closed loop feedback system between an intraluminally placed FOP-M260 pressure probe (FISO, Quebec, QC, Canada); a signal conditioner; a laptop with PID Pump Data Log software (Harvard Apparatus, Holliston, MA, USA) installed; and a PHD Ultra 703007 Syringe Pump (Harvard Apparatus, Holliston, MA, USA) equipped with a 50 mL syringe reservoir of PBS. Desired pressures were set on the laptop using the PID Pump Data Log software and maintained using this closed-loop feedback. Samples were given two minutes to equilibrate to each pressure step prior to imaging. Aortae were marked at three positions along the length of the vessel: 25% (proximal), 50% (middle/treated), and 75% (distal) using a permanent marker as shown in Figure 2b,c and vessel diameters were measured at each location using ImageJ analysis software. Following inflation, samples were rinsed in PBS, sectioned into 2 mm wide rings at the marked sites and fixed for histological analysis. The degree of dilation exhibited by the middle region at each pressure step was calculated separately by normalising the diameter measurement with respect to the initial middle diameter at 0 mmHg for absolute dilation and to the average diameter of the adjacent proximal and distal regions at that pressure step for relative dilation. Lastly, the physiological compliance was calculated as the change in absolute dilation over the 90–120 mmHg pressure range.

2.3. Histological Processing and Histomorphometric Quantification

After mechanical testing, all samples were fixed in 10% formalin solution (Sigma-Aldrich, Burlington, VT, USA) at 4 °C for 48 h, stepwise dehydrated using ethanol and xylene, and embedded in paraffin wax. Wax-embedded samples were sectioned along the transverse axis using a microtome (Leica Biosystems, Wetzlar, Germany) into 7 µm thick slices. Slides were stained with Verhoeff's elastic stain and imaged using an Aperio CS2 microscope installed with ImageScope software (V12.3.). QuPath (V0.2.3) image analysis software was used to quantify elastin content using a colour deconvolution approach comprising three distinct steps [52]. First, the RGB values defining stain colour (referred to as the stain vector) were determined from a subset of images. Next, a thresholder was defined to distinguish the tissue from the background in images. Lastly, using the stain vector, a separate thresholder was applied to identify the percentage surface area fraction of the tissue area stained for elastin (Equation (4)).

$$\%\text{Areafraction} = \frac{area\ stained\ for\ elastin}{tissue\ area} * 100 \quad (4)$$

Protocols for stain vector determination and tissue and stain thresholding were standardised for all measurements. For elastin quantification of individual rings, each ring was sectioned into four slices, each of which was assessed at three ROIs, and as such, the individual values for each ring represent the average of 12 individual measurements. Each ROI encompassed the full wall thickness.

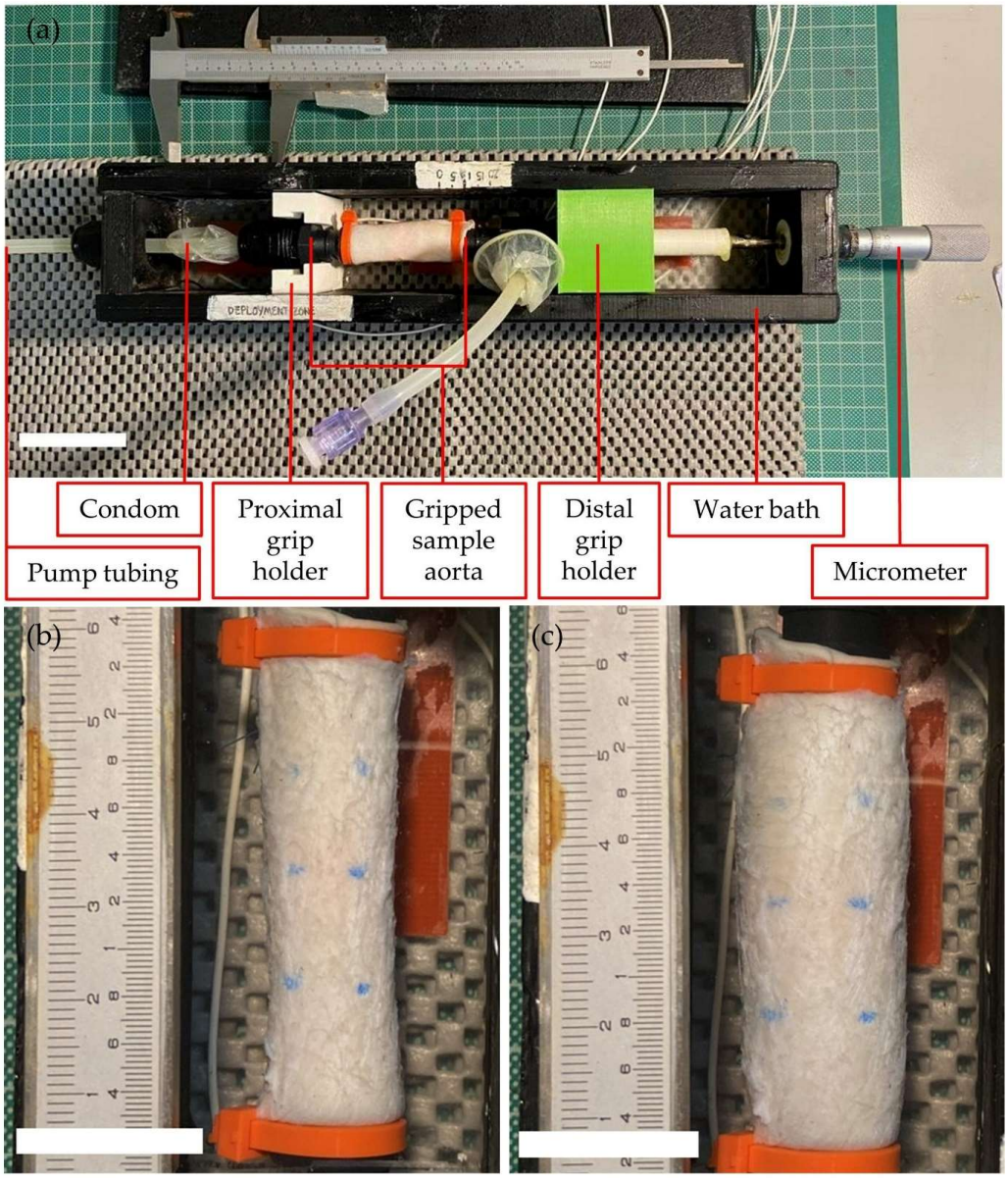

Figure 2. Inflation extension of whole porcine aorta. (**a**) Custom-made inflation-extension rig; scale bar represents 5 cm. Control treated aorta at (**b**) 0 mmHg and (**c**) 150 mmHg. Scale bars are 2 cm.

2.4. Statistical Analysis

Quantitative data are presented as mean and standard deviation. $p < 0.05$ was determined as the threshold of significance. Outliers were identified and removed using the ROUT method with a set maximum false discovery rate of 1% (Q = 1%). In the case of the presence of an outlier it is stated with the individual result. The Shapiro-Wilk normality test determined use of either a one-way ANOVA (parametric) or Kruskall-Wallis test (non-parametric) and post hoc comparisons were made with either Tukey's or Dunnett's correction for multiple comparisons, respectively. For one-way ANOVA, if the Brown-Forysthe test determined unequal standard deviations then Welch's correction was applied.

Due to the repeated nature of measures for dilation of whole aorta models, a two-way repeated measures ANOVA was performed for analyses of the absolute and relative dilation of the whole aorta models. For this analysis, sphericity was assumed and post-hoc comparisons were made using Šídák's multiple comparisons test. All statistical analyses were performed with GraphPad Prism software (V 9.3.1).

3. Results

3.1. Impact of Elastase Treatment on Aortic Elastin Structure and Content

Elastase treatment produced a time dependent degradation of elastin in porcine aortic rings. Verhoeff's elastin staining revealed partially degraded samples which were characterised by radially distinct regions: elastin-depleted inner and outer edges with an elastin-conserved medial region (Figure 3c). This clearly indicates that degradation occurred from enzyme-contacting surfaces moving radially inwards. The innermost medial elastin fibres were mainly conserved following 9 h of incubation, fragmented at 18 h, and completely absent following 27 h (Figure 3c–e). Elastin quantification confirmed the observed decreases in elastin content with increasing elastase incubation time (Figure 3f).

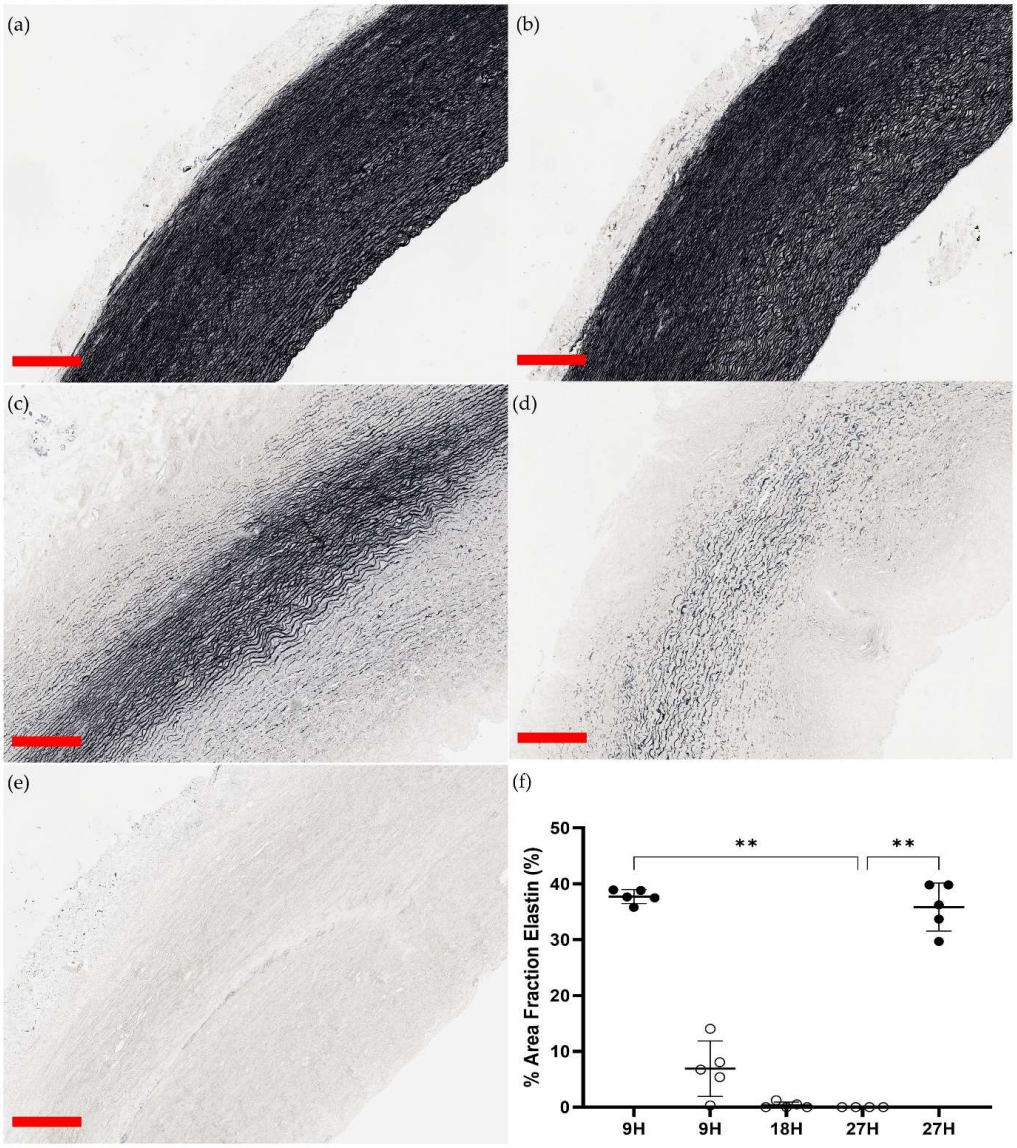

Figure 3. Qualitative and quantitative histological assessment of elastin content in aortic rings incubated in 1 U/mL of elastase or control solution over 9-, 18- and 27-h periods. Representative

histological slices for (**a**) the 9-h and (**b**) 27-h control groups; and (**c**) 9-, (**d**) 18- and (**e**) 27-h elastase-treated groups– all scale bars are 5 mm. (**f**) Measured elastin % Area fraction in each group. Black dots are control groups, whereas hollow circles are elastase treated groups; n = 5 for all groups except the 27-h elastase-treated group (n = 4) as one histological sample was lost in processing. Significance was determined via Kruskall-Wallis test and post hoc comparisons with Dunnett's correction (** $p < 0.01$).

3.2. Impact of Elastase Treatment on Aortic Ring Morphology

Enzymatic treatment with elastase produced progressive changes in aortic ring appearance and morphology with increasing incubation time as demonstrated in Figure 4a–e. Rings transformed from a well-defined tissue in control groups (Figure 4a,e) to semi-translucent, non-rigid, gel-like tissues seen in the 18- and 27-h elastase treated groups (Figure 4c,d). The average ring thickness and circumference significantly increased following 18- and 27-h elastase incubations (*** $p < 0.0001$), which reduced ring elastin content to less than 1% (Figure 3f). These changes contributed to increases in the average initial gauge length with elastase treatment from 17.3 ± 2.35 and 19.1 ± 1.25 mm in 9- and 27-h control groups, respectively, to 35.6 ± 3.43 mm in the 27-h treated group (*** $p = 0.0009$, ** $p = 0.008$) (Figure 4h). Increases in sample thickness and initial gauge length exhibited by samples exposed to longer enzyme incubation times contributed to increases in the force and displacement induced per unit stress and strain calculated for these samples in subsequent analyses.

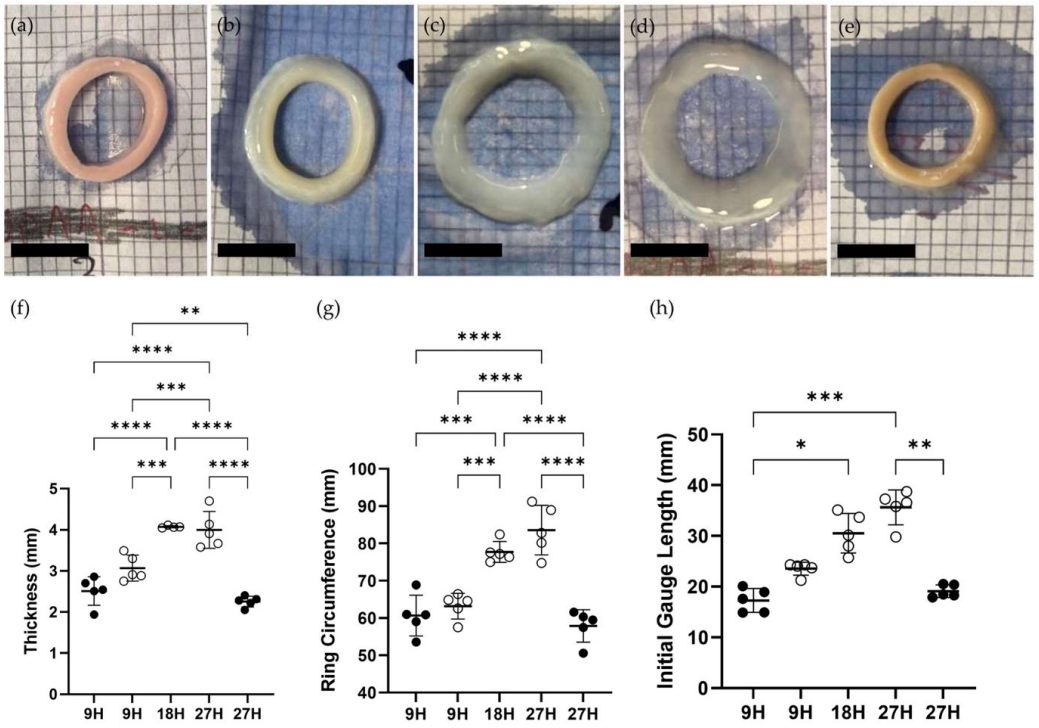

Figure 4. Morphological features of individual aortic rings incubated in either 1 U/mL elastase or control solution across 9-, 18- and 27-h intervals. Representative images of rings from the same pig from (**a**) the 9-h control, (**b**) 9-h elastase, (**c**) 18-h elastase, (**d**) 27-h elastase, and (**e**) 27-h control groups. Scale bars are 5 mm. For (**f**–**h**) black dots are control groups and hollow dots are elastase treated groups. (**f**) Measurements of ring thickness; one outlier was identified and removed from the 18-h elastase-treated group; significance determined via one way ANOVA with Welch's correction. (**g**) Measurements of ring circumference; one-way ANOVA was performed. (**h**) Recorded values for initial sample gauge length following preloading to 0.05 N during tensile testing. Kruskal-Wallis statistical analysis was performed. For (**f**–**h**): * $p < 0.05$, ** $p < 0.01$, *** $p < 0.001$, **** $p < 0.0001$.

3.3. Impact of Elastase Incubation on the Tensile Properties of Aortic Rings

Control rings at 9- and 27-h demonstrated the J-shaped stress-strain behaviour characteristic of arterial tissues (Figure 5a,b). The 9-h elastase treatment group demonstrated a decrease in resistance to initial deformation evidenced by a flattening of the initial portion of the curve followed by more rapid stiffening (Figure 5c). Rings treated for 18- and 27-h (Figure 5d,e) further demonstrated a decrease in initial stiffness and increase in the final slope of the curve; stiffening also occurred at lower strains in these groups. The strain at which stiffening occurred varied widely in the 18-h elastase treated group (Figure 5d). The 27-h elastase treated group, which contained virtually no elastin, as seen in Figure 3c, demonstrated very stiff behaviour almost immediately upon sample loading. Of note, the small flat region at the beginning of these curves is consistent with the 10% strain range over which samples were preconditioned prior to testing as highlighted in Supplementary Figure S1. Overall, elastase incubation induced progressive decreases in the initial resistance to deformation followed by progressively earlier and more rapid stiffening.

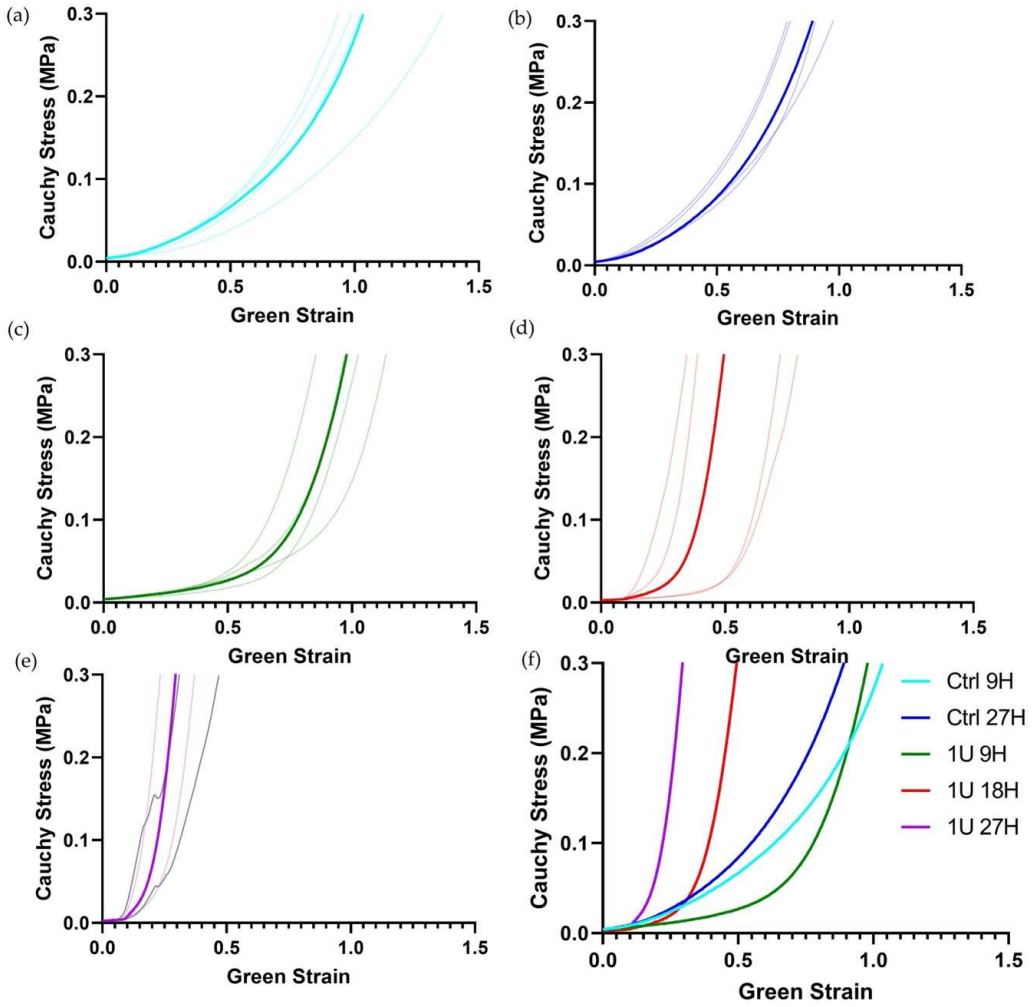

Figure 5. Cauchy stress-Green strain data from ring testing of control (Ctrl) and elastase (1 U/mL) treated samples at 9-, 18- and 27-h. Data on graphs is color-coded by treatment group and all curves for each treatment group are shown with the median curve highlighted in bold. Cauchy stress-Green strain data is presented for (**a**) the 9-h control, (**b**) 27-h control, (**c**) 9-h elastase, (**d**) 18-h elastase, and (**e**) 27-h elastase treatment groups. Stress strain curves from two rings in the 27-h group, coloured in grey, were excluded from further analyses due to yielding prior to 300 kPa Cauchy stress—seen by the sharp dips in the curves. (**f**) The median curves from all groups are reproduced for comparison.

Quantitative analyses of stress-strain behaviour in the initial and final regions of the stress-strain curves in Figure 5 are shown in Figure 6. First, the initial tangent moduli confirmed observations of progressive decreases in resistance to initial deformation upon loading with decreasing elastin content up to the 18-h incubation time. Notably, the 27-h control group demonstrated increased initial moduli compared to the 9-h control group, further highlighting that the decreases seen in the elastase treated groups are due to elastin depletion. The final tangent moduli saw significant increases with increasing elastase incubation time from 0.71 ± 0.114 and 0.88 ± 0.133 MPa in the 9- and 27-h controls, respectively, to 3.30 ± 0.348 MPa in the 27-h treatment group. Elastase treatment induced time-dependent decreases in initial stiffness and concomitant increases in final stiffness in rings of porcine aorta.

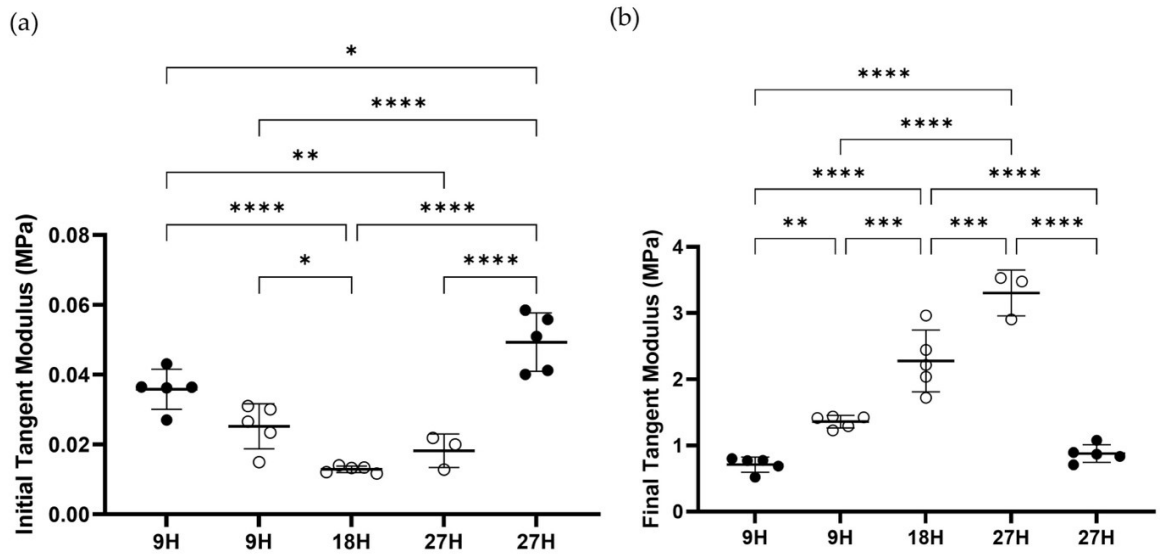

Figure 6. Analysis of stress-strain behaviour of rings. Black dots are control groups, whereas hollow circles are elastase treated groups. Tangent moduli for the initial and final stages of ring loading are plotted in (**a**,**b**), respectively. Statistical analyses were performed using one-way ANOVA (* $p < 0.05$, ** $p < 0.01$, *** $p < 0.001$, **** $p < 0.0001$).

Treatment with elastase resulted in a notable reduction in the strain level achieved at the maximum stress applied of 300 kPa, particularly in the 18- and 27-h elastase treated samples (Figure 7a). However, analysis of the pin-to-pin distance (proxy for circumferential length) at the maximum stress revealed that elastase treatment caused a significant increase in circumferential length: from 31.7 ± 3.69 (9-h control) and 32.6 ± 1.31 mm (27-h control) to 41.9 ± 3.49 mm in the 9-h elastase treatment group, which was also present for the longer incubation times (Figure 7b). As such, while near complete elastin degradation caused stiffening to occur at lower strains, elastase-treated rings demonstrated significantly increased initial sample gauge lengths (Figure 4h) resulting in these stiffer samples actually reaching higher final lengths at 300 kPa compared to the control samples. These findings highlight that progressive elastase treatment can be used to produce porcine aortic tissues with increased arterial diameter and progressive increases in stiffness across a given stress range (0.25–0.3 MPa in this instance). Thus, there exists a threshold level of elastin degradation at which porcine aortic tissues demonstrate a greater arterial diameter and increased mural stiffness similar to those seen in AA under physiological stresses.

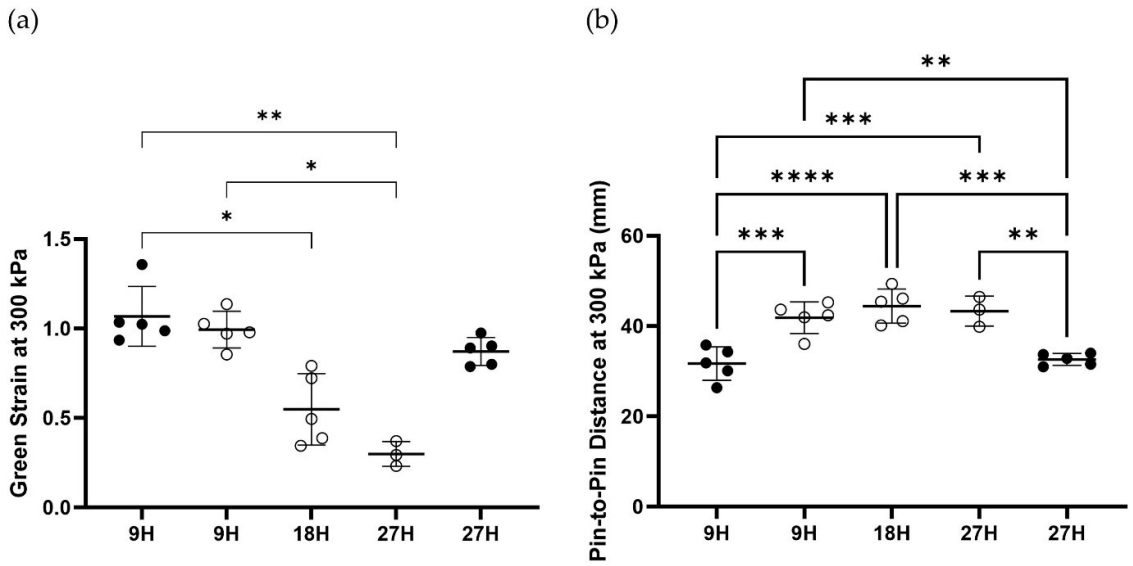

Figure 7. The (**a**) green strain and (**b**) pin-to-pin distance of aortic rings at 300 kPa Cauchy stress. Black dots are control groups, whereas hollow circles are elastase treated groups. Statistical analyses were performed using Kruskall-Wallis and one-way ANOVA for (**a**) and (**b**), respectively; (* $p < 0.05$, ** $p < 0.01$, *** $p < 0.001$, **** $p < 0.0001$).

3.4. Ex Vivo Porcine Model with Localised Elastin Degradation

Spatially controlled elastin degradation of a 1 cm portion of 6 cm long aortic segments was produced by localised exposure to elastase. Representative Verhoeff's elastin-stained sections of rings cut at proximal, middle (treated) and distal positions along the vessel length for one aorta from each group are shown in Figure 8. These demonstrate spatially controlled elastin degradation which was limited to the treated segment of the aortae (Figure 8e–f). All other samples in the control and treatment groups can be seen in Supplementary Figures S2 and S3. The mid-sections (treated) of the elastase-treated aortae (Figure 8e) exhibit less elastin degradation compared to the aortic rings (Figure 3c) exposed to the same 9-h treatment protocol.

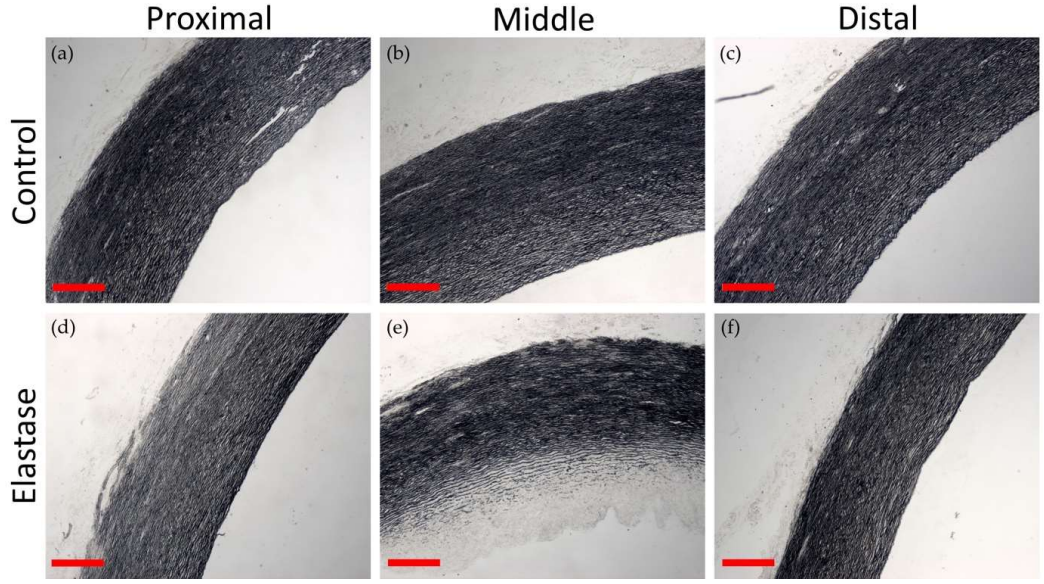

Figure 8. Representative histology of local elastin degradation in a whole porcine aortic segment. Verhoeff's elastin-stained slices taken from (**a**,**d**) proximal, (**b**,**e**) middle (treated), and (**c**,**f**) distal regions of representative control (**a**–**c**) and elastase-treated (**d**–**f**) aortae. All scale bars are 500 µm.

3.5. Inflation-Extension of the Localised Elastin-Degradation Ex Vivo Aneurysm Model

The spatially controlled elastin degradation produced a localised increase in aortic dilation, but no significant change in stiffness under physiological pressures (90–120 mmHg) (Figure 9). The elastase-treated region of the aortae demonstrated a small but significant (* $p = 0.047$) increase in absolute dilation compared to control-treated aortae, Figure 9a. Furthermore, the treated regions of elastase-treated aortae demonstrated a significantly (* $p = 0.017$) increased relative dilation (diameter normalised with respect to the untreated proximal and distal regions) compared to that of the control aortae, Figure 9b. However, this increased dilation did not yield any significant change in physiological arterial compliance (the change in absolute dilation across 90–120 mmHg), Figure 9c.

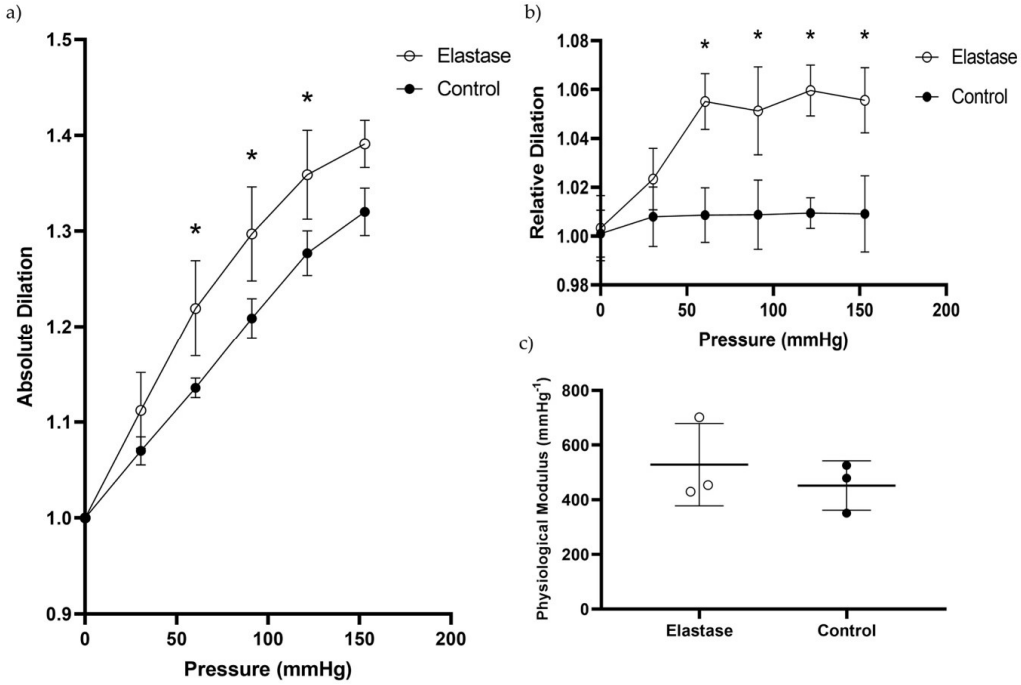

Figure 9. Inflation-extension of whole porcine aortae with localised elastin degradation. Black dots are control aortae, whereas hollow circles have elastase treatment. (**a**) Absolute dilation (normalised to diameter at 0 mmHg) at the middle region for each aorta with respect to pressure. (**b**) Relative dilation (normalised to average diameter between adjacent untreated proximal and distal regions) of the middle region with respect to pressure. Significance was determined by a 2-way repeated measures ANOVA with Šídák's multiple comparisons; (* $p < 0.05$). (**c**) No significant difference was seen in physiological (90–120 mmHg) compliance. All data is presented with mean and standard deviation, n = 3 aortae per group.

This increased dilation is consistent with the mechanical data from the ring tests in which elastase treatment produced increases in arterial diameter under the same applied tension. However, the lack of change in stiffness indicates that the increase in aortic deformation produced at this level of elastin degradation was below the threshold at which strain-induced stiffening occurs. Overall, elastase treatment was still able to induce localised changes in pressure-diameter behaviour which are consistent with those seen in the ring analysis.

4. Discussion

Elastase treatment induced increases in the circumferential length and tensile modulus in rings of porcine aortae when compared to untreated controls, similar to that seen in AA. Using insight from these elastase-treated ring samples, we established a local elastin degradation protocol for whole aortae which caused localised dilation under physiological

pressures, similar to that seen in AA. These findings highlight a promising avenue to use localised elastin degradation to produce an ex vivo aneurysm model.

Elastase-treated aortic rings demonstrated significant increases in circumferential length both in the unloaded state (Figure 4h) and under 300 kPa Cauchy stress (Figure 7b), results which are consistent with findings from other groups [22,39–41,53]. In healthy tissues, resistance to deformation is provided by the initial recruitment of pliable elastin fibres followed by the progressive recruitment of stiff collagen fibres with increasing strain [16,54]. This strain-dependent recruitment is permitted by the wavy 'crimped' architecture of groups of collagen fibres allowing them to be 'pulled taut' and thus recruited at specific levels of tissue deformation [22,55]. Using a multiphoton microscopy approach, Chow et al. found that elastase-induced increases in the loaded length of porcine aortic tissues were attributed to increases in collagen fibre uncrimping with respect to untreated controls under the same conditions of stress similar to that seen in mechanical loading in untreated tissues [22,55]. As such, elastase-induced increases in loaded length result from the increased deformation required to recruit sufficient collagen fibres to make up for decreases in elastin mediated resistance [22,53]. Additionally, the increases in unloaded circumference seen in the highly depleted elastin aortic rings indicates that collagen crimp in unloaded arterial tissues is maintained by a compressive force imposed by the elastic fibres in the resting state [16,40,53]. As such, elastase-mediated increases in unloaded length secondary to a loss in elastin-mediated compression act similar to an 'initial stretch' on the collagenous architecture in the unloaded state compared to untreated tissues. This stretching nature of elastase-induced increases in unloaded circumferential length is recognised by groups such as Chow et al. in porcine aortae and Fonck et al. in rabbit carotids [41,53]. Overall, increases in aortic circumferential length due to elastase treatment in both loaded and unloaded configurations are attributed to the increased stretch, and thus decreased crimp, exhibited by collagen fibres under the same load in elastin depleted tissues. This work builds upon existing literature to highlight the role of elastic fibres in mediating vessel circumference and compliance in loaded and unloaded states through their role in preserving collagen crimp.

Elastase treatment induced increased compliance under low stress, and increased stiffness under high stress in rings of porcine aorta. Chow et al. found that the tensile properties of porcine aortae incubated in elastase solution progressed through distinct sequential stages of 'initial softening' characterised by a flattening of the initial region of the curve; 'extensible but stiff' behaviour characterised by an increase in the slope of the final region; and 'collagen scaffold'-like behaviour characterised by immediate stiffening upon loading with increasing elastase incubation time similar to that seen in our study [41]. Furthermore, these findings are in line with those of Fonck et al. who report that elastase-treated rabbit carotids were more pliable under low circumferential stretch and less pliable under higher circumferential stretch [53]. Decreases in initial stiffness are attributed to reductions in the number and integrity of elastic fibres present to provide resistance to initial deformation with increasing elastase incubation time [16,41].

However, while elastase treatment induced significant increases in loaded and unloaded circumferential length, measured increases in circumferential length fall short of the 50% dilation exhibited in human aneurysms [1]. Kratzberg et al. reported that application of a creep loading protocol produced a further plastic deformation of 23.6 $\pm$ 10.5% and 22.5 $\pm$ 7.1% in partially and completely elastin-depleted strips of porcine aorta, respectively [40]. Perhaps application of a similar creep loading approach would increase dilation to similar levels in the ex vivo porcine aortae to yield the 50% dilation pathognomonic of human aneurysms.

Elastin degradation represents a feasible method to produce porcine aortic tissues with similar compliance to human AA. Significant heterogeneity with regards to testing and analysis methodologies used to quantify the tensile properties of human AA in the literature limits direct comparison of measured values [56]. Individual studies indicate that human TAA and AAA demonstrate respective increases in circumferential stiffness of

44% and 60% compared to healthy human aortae under the same degree of stress [18,57]. Notably, a comparative analysis conducted by de Beaufort et al. found that healthy porcine aortae demonstrated similar compliance to aortae from young humans under 100 mmHg of pressure, but only 41% of the stiffness found in aortae from humans over 60 years of age [31]—in which aneurysms most frequently occur [58]. This indicates that human AAA and TAA may have 350 and 390% greater circumferential stiffness, respectively, compared to healthy porcine aortae. Elastase treatments conducted as part of this study produced dramatic increases in the circumferential stiffness of rings of porcine aorta with rings in the 27-h treatment group demonstrating a 380% increased circumferential stiffness compared to time-matched controls over a Cauchy stress range of 250–300 kPa. A follow-up study including mechanical assessments of aneurysmal human and elastin-depleted porcine aortae would allow optimisation of elastase incubation time to produce porcine aortic models with similar stiffness to that seen in human aneurysms.

The proposed ex vivo locally elastin-depleted porcine aorta model represents a more comprehensive non-living model than those currently available. Non-living models of aortic aneurysm can be subclassified, based on their material composition, as ex vivo, in vitro synthetic, in vitro tissue-based, and in silico. First, this model recapitulates the dilation and stiffening seen in aortic aneurysms not demonstrated in the ex vivo healthy porcine aorta model [27–31]. Next, while in vitro synthetic models offer high geometric accuracy and patient-specificity, the synthetic polymers used poorly replicate the compliance and failure mechanics of arterial tissues [20,32–35]. Conversely, in vitro tissue-based models offer accurate replication of the macro and microstructural features of aortic aneurysms, however their production is highly resource intensive and has not yet been achieved on a scale suitable for endovascular device testing [36–38]. Lastly, in silico models use solid mechanics and fluid mechanics simulation platforms, in conjunction with material and geometrical data to model the behaviour of the aortic wall, blood, and stent-graft components across preclinical, and clinical settings [15,19]. However, the accuracy of predictions generated from these models depends on the fidelity of the selected model equations, assumptions, and boundary conditions; alongside the accuracy of the experimentally-derived parameters such as aortic wall geometry and compliance [15,19]. Ultimately, this methodology is limited by its greater degree of abstraction from the clinical in vivo setting compared to in vitro physical models [15,19]. Overall, the proposed ex vivo locally elastin-depleted porcine aorta model meets an existing need for a tissue-based non-living physical model which recapitulates the geometric and mechanical properties of the aneurysmal aortic wall.

The model produced and characterised as part of this work demonstrates several key advantages. First, the proposed model meets an established need for an ex vivo large animal model representative of the geometric and compliance features of aneurysms suitable for endovascular device testing. It represents a comprehensive reproduction of the mechanical features of aneurysm and its use could facilitate better testing and optimisation of endovascular devices prior to in vivo testing. Second, the produced model can be directly assembled from widely available low-cost parts allowing for rapid production and use. Lastly, this approach can produce models of aneurysms demonstrating distinct geometric or anatomical features, e.g., aortic root or arch aneurysms, facilitating the improvement of endovascular treatments in these areas [7]. Overall, our proposed model demonstrates clear advantages: it replicates the mechanical features of AA better than existing in vitro models; requires minimal skill and resource requirements; and has the potential for customisability to specific aneurysm pathologies.

However, the produced model requires further optimisation prior to its progression in the testing of endovascular devices. The degree of elastin degradation produced in whole aortae as part of this work resulted in an approximate 5% increase in dilation and no change in compliance under physiological pressures compared to controls. Human aneurysms demonstrate a 50% increased diameter [1] and a 44% and 60% increased circumferential stiffness at thoracic or abdominal locations, respectively, compared to non-aneurysmal aortae [18,57]. While our findings are consistent with the level of degradation seen, a larger

degree of elastin degradation is needed to produce a more physiologically relevant model. Furthermore, the 1 cm length utilized as part of this study is not representative of the lengths of aneurysmal dilation in human aneurysms [59]. Reproduction of our localised degradation over a longer time period and larger aortic segment, would produce a model more robust for use in endovascular device testing.

This work is subject to several methodological limitations. First, the studied group is relatively small comprising samples from 5 animals in the ring analysis and 6 animals in the whole-aorta analysis. However, while the sample number was low, experiments were sufficiently powered to observe statistically meaningful differences. Second, use of an enzyme-soaking method limited direct translation of the 9-h elastase treatment protocol directly from ring-samples to whole aortae in this work most likely due to differences in the exposed surface area to volume ratio. This method was selected for use in this work due to its simplicity and its successful use in relevant background literature to produce the desired changes in arterial geometry and compliance [22,40,41,53]. Future work will explore the importance of controlling diffusion parameters such as the ratio of exposed sample surface area to volume ratio, between experiments when using this technique. The formation of a translucent gelatinous precipitate on elastin-depleted rings impacted the accuracy with which unloaded sample dimensions could be measured optically. This finding has been reported by other groups and was minimised in this study by imaging each ring against a high contrast graph paper background and with the light source at different positions [41,60]. Histomorphometric quantifications of constituent composition are sensitive to variations in selected image analysis parameters and component staining lending a subjective component to obtained values [61]. To maximise measurement objectivity, all samples in this study were prepared and analysed in the same manner [61]. Use of this method in this study offered several advantages including semi-quantitative assessment of the time-degradation relationship, the variability of produced degradations, and is consistent with work performed by other groups in this field [17,18,24,62]. Use of pins with a smaller radius than the vessel thickness may have contributed to stress concentrations at the pins predisposing to tissue failure at these points [63]. As such, the failure characteristics of analysed tissues were not assessed as part of this study. Lastly, this study utilised measures of average strain such as crosshead displacement and video extensometry in ring tensile and inflation extension testing, respectively, rather than more resource-intensive measures of local strain such as those employed by Shazly et al. and Lane et al. [42,64]. This work chose to measure average strain as this was appropriate for the characterisation of a segmentally homogenous approximate model of overall aneurysmal pressure-dilation behaviour [48]. Furthermore, cross-head displacement and video extensometry are validated accurate measures of average strain and are utilised widely by other groups [17,48,51].

Endovascular aortic repair represents the preferred management of AA in the elective setting and is becoming increasingly popular in the treatment of aortic rupture [4–6]. However, the early benefits of EVAR in morbidity and mortality over open surgical repair in the elective setting are lost after 3 years due to high rates of post-procedural device-related complications such as endoleaks and device migration [4]. The development of better in vitro models represents a useful tool to allow the refinement of device designs to optimise these factors prior to costly in vivo trials. Of these, ex vivo animal models allow for the most comprehensive representation of aortic mechanics replicating both the non-linear stress-strain and material failure behaviours such as endothelial injury, aortic dissection, and rupture - all of which are not possible with synthetic models [20,65]. However, as of yet, no model representative of the dilation and stiffening seen in AA exists on a scale suitable for ex vivo endovascular device testing. Our ex vivo model using whole porcine aortae with localised elastin degradation represents a promising avenue to address this need. Our model could facilitate new device designs leading to further reductions in the morbidity and mortality of AA through improvements in endovascular device applications and performance.

5. Conclusions

This work assessed the feasibility of a localised elastin degradation approach in porcine aortae to produce an ex vivo model of AA suitable for the testing of endovascular devices. Elastase treatment of aortic rings produced time-dependent decreases in elastin content and resulted in significant changes in morphological and tensile properties. Elastase-treated rings demonstrated increases in loaded circumferential length and mural stiffness similar to those seen in human aneurysms. Following from this, elastase treatment was successfully localised to segments of whole porcine aortae. Elastase treatment produced significant changes in local pressure-diameter behaviour compared to untreated aortae which was consistent with the level of degradation produced. Overall, a localised elastin degradation of porcine aortic segments represents a feasible method to produce aortae which better exhibit the local dilation and stiffening seen in human aneurysms than what is seen in existing models. Use of our physiologically relevant ex vivo model of AA in the design and optimisation of endovascular devices has the potential to alter the current benchtop test beds for such devices and ultimately contribute to reductions in the morbidity and mortality of AA.

Supplementary Materials: The following supporting information can be downloaded at: https://www.mdpi.com/article/10.3390/app13179894/s1: Figure S1: Cauchy stress-Green strain behaviour of a single representative sample from the 27-h elastase-treated group over five preconditioning cycles to 10% engineering strain before being stretched to failure; Figure S2: representative Verhoeff's elastin stained slices at proximal, middle and distal sites from whole aortae (n = 3) treated with control solution (DMEM) for 9 h; Figure S3: representative Verhoeff's elastin stained slices at proximal, middle (treated), and distal sites from whole aortae (n = 3) treated with elastase solution for 9 h. (a–c) and (d–f) demonstrate sections cut from the second and third aortae treated respectively.

Author Contributions: A summary of author contributions to the presented work is provided: conceptualization, B.T. and C.L.; methodology, B.T. and M.L.; validation, M.L.; formal analysis, M.L.; investigation, M.L.; resources, B.T., M.L. and C.L.; data curation, M.L.; writing—original draft preparation, M.L.; writing—review and editing, B.T. and C.L.; supervision, B.T. and C.L.; project administration, C.L. All authors have read and agreed to the published version of the manuscript.

Funding: This research was supported by the European Research Council (ERC) under the European Union's Horizon 2020 research innovation programme (grant agreement no. 637674).

Institutional Review Board Statement: Ethical review and approval were waived for this study as all animal tissues used were obtained following death at a licensed abattoir.

Informed Consent Statement: Not applicable.

Data Availability Statement: The data presented in this study is available upon reasonable request.

Acknowledgments: The authors would like to acknowledge Robert Johnston, Yasmine Guendouz, and Adeebah Razif within the Trinity College Cardiovascular Biomechanics research group for their input on design iterations of the developed 3D printed rigs used in this work.

Conflicts of Interest: The authors declare no conflict of interest.

Abbreviations

AA—Aortic Aneurysm; TAA—Thoracic Aortic Aneurysm; AAA—Abdominal Aortic Aneurysm; PBS—Phosphate Buffered Saline; DMEM—Dulbecco's modified eagle medium; PLA—Polylactic Acid; RGB—Red Green Blue.

References

1. Tse, H.-F.; Lip, G.Y.; Coats, A.J.S. *Cardiology (Oxford Desk Reference)*; Oxford University Press: Oxford, UK, 2011.
2. Li, X.; Zhao, G.; Zhang, J.; Duan, Z.; Xin, S. Prevalence and Trends of the Abdominal Aortic Aneurysms Epidemic in General Population—A Meta-Analysis. *PLoS ONE* **2013**, *8*, e81260. [CrossRef]
3. Wei, L.; Bu, X.; Wang, X.; Liu, J.; Ma, A.; Wang, T. Global Burden of Aortic Aneurysm and Attributable Risk Factors from 1990 to 2017. *Glob. Heart* **2021**, *16*, 35. [CrossRef]

4. Powell, J.T.; Sweeting, M.J.; Ulug, P.; Blankensteijn, J.D.; Lederle, F.A.; Becquemin, J.P.; Greenhalgh, R.M. Meta-analysis of individual-patient data from EVAR-1, DREAM, OVER and ACE trials comparing outcomes of endovascular or open repair for abdominal aortic aneurysm over 5 years. *Br. J. Surg.* **2017**, *104*, 166–178. [CrossRef]
5. Lilja, F.; Wanhainen, A.; Mani, K. Changes in abdominal aortic aneurysm epidemiology. *J. Cardiovasc. Surg.* **2017**, *58*, 848–853. [CrossRef]
6. Alsusa, H.; Shahid, A.; Antoniou, G.A. A comparison of endovascular versus open repair for ruptured abdominal aortic aneurysm—Meta-analysis of propensity score-matched data. *Vascular* **2022**, *30*, 628–638. [CrossRef]
7. Daye, D.; Walker, T.G. Complications of endovascular aneurysm repair of the thoracic and abdominal aorta: Evaluation and management. *Cardiovasc. Diagn. Ther.* **2018**, *8* (Suppl. 1), S138–S156. [CrossRef] [PubMed]
8. Hirsch, A.T.; Haskal, Z.J.; Hertzer, N.R.; Bakal, C.W.; Creager, M.A.; Halperin, J.L.; Hiratzka, L.F.; Murphy, W.R.; Olin, J.W.; Puschett, J.B.; et al. ACC/AHA 2005 Practice Guidelines for the management of patients with peripheral arterial disease (lower extremity, renal, mesenteric, and abdominal aortic): A collaborative report from the American Association for Vascular Surgery/Society for Vascular Surgery, Society for Cardiovascular Angiography and Interventions, Society for Vascular Medicine and Biology, Society of Interventional Radiology, and the ACC/AHA Task Force on Practice Guidelines (Writing Committee to Develop Guidelines for the Management of Patients With Peripheral Arterial Disease): Endorsed by the American Association of Cardiovascular and Pulmonary Rehabilitation; National Heart, Lung, and Blood Institute; Society for Vascular Nursing; TransAtlantic Inter-Society Consensus; and Vascular Disease Foundation. *Circulation* **2006**, *113*, e463–e654. [CrossRef]
9. Cernohorsky, P.; Reijnen, M.M.; Tielliu, I.F.; van Sterkenburg, S.M.; van den Dungen, J.J.; Zeebregts, C.J. The relevance of aortic endograft prosthetic infection. *J. Vasc. Surg.* **2011**, *54*, 327–333. [CrossRef] [PubMed]
10. Makaroun, M.S.; Dillavou, E.D.; Wheatley, G.H.; Cambria, R.P. Five-year results of endovascular treatment with the Gore TAG device compared with open repair of thoracic aortic aneurysms. *J. Vasc. Surg.* **2008**, *47*, 912–918. [CrossRef] [PubMed]
11. Dake, M.D.; Miller, D.C.; Mitchell, R.S.; Semba, C.P.; Moore, K.A.; Sakai, T. The "first generation" of endovascular stent-grafts for patients with aneurysms of the descending thoracic aorta. *J. Thorac. Cardiovasc. Surg.* **1998**, *116*, 689–703; discussion 684–703. [CrossRef]
12. Liaw, J.V.P.; Clark, M.; Gibbs, R.; Jenkins, M.; Cheshire, N.; Hamady, M. Update: Complications and management of infrarenal EVAR. *Eur. J. Radiol.* **2009**, *71*, 541–551. [CrossRef]
13. Bavaria, J.E.; Appoo, J.J.; Makaroun, M.S.; Verter, J.; Yu, Z.F.; Mitchell, R.S. Endovascular stent grafting versus open surgical repair of descending thoracic aortic aneurysms in low-risk patients: A multicenter comparative trial. *J. Thorac. Cardiovasc. Surg.* **2007**, *133*, 369–377. [CrossRef]
14. Laheij, R.J.F.; Buth, J.; Harris, P.L.; Moll, F.L.; Stelter, W.J.; Verhoeven, E.L.G. Need for secondary interventions after endovascular repair of abdominal aortic aneurysms. Intermediate-term follow-up results of a European collaborative registry (EUROSTAR). *BJS (Br. J. Surg.)* **2000**, *87*, 1666–1673. [CrossRef]
15. Avril, S.; Gee, M.W.; Hemmler, A.; Rugonyi, S. Patient-specific computational modeling of endovascular aneurysm repair: State of the art and future directions. *Int. J. Numer. Methods Biomed. Eng.* **2021**, *37*, e3529. [CrossRef]
16. Roach, M.R.; Burton, A.C. The reason for the shape of the distensibility curves of arteries. *Can. J. Biochem. Physiol.* **1957**, *35*, 681–690. [CrossRef]
17. Iliopoulos, D.C.; Kritharis, E.P.; Giagini, A.T.; Papadodima, S.A.; Sokolis, D.P. Ascending thoracic aortic aneurysms are associated with compositional remodeling and vessel stiffening but not weakening in age-matched subjects. *J. Thorac. Cardiovasc. Surg.* **2009**, *137*, 101–109. [CrossRef]
18. He, C.M.; Roach, M.R. The composition and mechanical properties of abdominal aortic aneurysms. *J. Vasc. Surg.* **1994**, *20*, 6–13. [CrossRef]
19. Cebull, H.L.; Rayz, V.L.; Goergen, C.J. Recent Advances in Biomechanical Characterization of Thoracic Aortic Aneurysms. *Front. Cardiovasc. Med.* **2020**, *7*, 75. [CrossRef]
20. Marconi, S.; Lanzarone, E.; van Bogerijen, G.H.W.; Conti, M.; Secchi, F.; Trimarchi, S.; Auricchio, F. A compliant aortic model for in vitro simulations: Design and manufacturing process. *Med. Eng. Phys.* **2018**, *59*, 21–29. [CrossRef]
21. Holzapfel, G.A.; Weizsäcker, H.W. Biomechanical behavior of the arterial wall and its numerical characterization. *Comput. Biol. Med.* **1998**, *28*, 377–392. [CrossRef]
22. Chow, M.J.; Turcotte, R.; Lin, C.P.; Zhang, Y. Arterial extracellular matrix: A mechanobiological study of the contributions and interactions of elastin and collagen. *Biophys. J.* **2014**, *106*, 2684–2692. [CrossRef]
23. Vande Geest, J.P.; Sacks, M.S.; Vorp, D.A. The effects of aneurysm on the biaxial mechanical behavior of human abdominal aorta. *J. Biomech.* **2006**, *39*, 1324–1334. [CrossRef] [PubMed]
24. Sokolis, D.P.; Kritharis, E.P.; Giagini, A.T.; Lampropoulos, K.M.; Papadodima, S.A.; Iliopoulos, D.C. Biomechanical response of ascending thoracic aortic aneurysms: Association with structural remodelling. *Comput. Methods Biomech. Biomed. Eng.* **2012**, *15*, 231–248. [CrossRef] [PubMed]
25. Yoffe, B.; Vaysbeyn, I.; Urin, Y.; Waysbeyn, I.; Zubkova, O.; Chernyavskiy, V.; Ben-Dor, D. Experimental Study of a Novel Suture-less Aortic Anastomotic Device. *Eur. J. Vasc. Endovasc. Surg.* **2007**, *34*, 79–86. [CrossRef]
26. Giannatsis, J.; Dedoussis, V. Additive fabrication technologies applied to medicine and health care: A review. *Int. J. Adv. Manuf. Technol.* **2009**, *40*, 116–127. [CrossRef]

27. de Beaufort, H.W.L.; Conti, M.; Kamman, A.V.; Nauta, F.J.H.; Lanzarone, E.; Moll, F.L.; van Herwaarden, J.A.; Auricchio, F.; Trimarchi, S. Stent-Graft Deployment Increases Aortic Stiffness in an Ex Vivo Porcine Model. *Ann. Vasc. Surg.* **2017**, *43*, 302–308. [CrossRef]
28. Nauta, F.J.H.; de Beaufort, H.W.L.; Conti, M.; Marconi, S.; Kamman, A.V.; Ferrara, A.; van Herwaarden, J.A.; Moll, F.L.; Auricchio, F.; Trimarchi, S. Impact of thoracic endovascular aortic repair on radial strain in an ex vivo porcine model. *Eur. J. Cardiothorac. Surg.* **2017**, *51*, 783–789. [CrossRef] [PubMed]
29. Nauta, F.J.; Conti, M.; Marconi, S.; Kamman, A.V.; Alaimo, G.; Morganti, S.; Ferrara, A.; van Herwaarden, J.A.; Moll, F.L.; Auricchio, F.; et al. An experimental investigation of the impact of thoracic endovascular aortic repair on longitudinal strain. *Eur. J. Cardiothorac. Surg.* **2016**, *50*, 955–961. [CrossRef]
30. de Beaufort, H.W.L.; Coda, M.; Conti, M.; van Bakel, T.M.J.; Nauta, F.J.H.; Lanzarone, E.; Moll, F.L.; van Herwaarden, J.A.; Auricchio, F.; Trimarchi, S. Changes in aortic pulse wave velocity of four thoracic aortic stent grafts in an ex vivo porcine model. *PLoS ONE* **2017**, *12*, e0186080. [CrossRef]
31. de Beaufort, H.W.L.; Ferrara, A.; Conti, M.; Moll, F.L.; van Herwaarden, J.A.; Figueroa, C.A.; Bismuth, J.; Auricchio, F.; Trimarchi, S. Comparative Analysis of Porcine and Human Thoracic Aortic Stiffness. *Eur. J. Vasc. Endovasc. Surg.* **2018**, *55*, 560–566. [CrossRef] [PubMed]
32. Hoefer, A.C.; Bouchagiar, J.; Goltz, J.P.; Horn, M.; Matthiensen, S.; Matysiak, F.; Stahlberg, E.; Kleemann, M. Development of an Endovascular Training Model for Simulation of Evar Procedures Using 3D Rapid Prototyping for the Production of Exchangeable Patient Specific Anatomic Models. *Eur. J. Vasc. Endovasc. Surg.* **2019**, *58*, e290–e292. [CrossRef]
33. Biglino, G.; Verschueren, P.; Zegels, R.; Taylor, A.M.; Schievano, S. Rapid prototyping compliant arterial phantoms for in-vitro studies and device testing. *J. Cardiovasc. Magn. Reson.* **2013**, *15*, 2. [CrossRef]
34. Doyle, B.J.; Morris, L.G.; Callanan, A.; Kelly, P.; Vorp, D.A.; McGloughlin, T.M. 3D Reconstruction and Manufacture of Real Abdominal Aortic Aneurysms: From CT Scan to Silicone Model. *J. Biomech. Eng.* **2008**, *130*, 034501. [CrossRef]
35. Sulaiman, A.; Boussel, L.; Taconnet, F.; Serfaty, J.M.; Alsaid, H.; Attia, C.; Huet, L.; Douek, P. In vitro non-rigid life-size model of aortic arch aneurysm for endovascular prosthesis assessment. *Eur. J. Cardio-Thorac. Surg.* **2008**, *33*, 53–57. [CrossRef]
36. Bianco, R.; Di Gregoli, K.; Caputo, M.; George, S.J.; Johnson, J.L. A Protocol for a Novel Human Ex Vivo Model of Aneurysm. *STAR Protoc.* **2020**, *1*, 100108. [CrossRef]
37. Bianco, R.; Di Gregoli, K.; Caputo, M.; Zakkar, M.; George, S.; Johnson, J. Development and characterisation of a human ex-vivo model of aneurysm. *Atherosclerosis* **2018**, *275*, e144–e145. [CrossRef]
38. Meekel, J.P.; Groeneveld, M.E.; Bogunovic, N.; Keekstra, N.; Musters, R.J.P.; Zandieh-Doulabi, B.; Pals, G.; Micha, D.; Niessen, H.W.M.; Wiersema, A.M.; et al. An in vitro method to keep human aortic tissue sections functionally and structurally intact. *Sci. Rep.* **2018**, *8*, 8094. [CrossRef]
39. Dobrin, P.B.; Mrkvicka, R. Failure of Elastin or Collagen as Possible Critical Connective Tissue Alterations Underlying Aneurysmal Dilatation. *Cardiovasc. Surg.* **1994**, *2*, 484–488. [CrossRef]
40. Kratzberg, J.A.; Walker, P.J.; Rikkers, E.; Raghavan, M.L. The effect of proteolytic treatment on plastic deformation of porcine aortic tissue. *J. Mech. Behav. Biomed. Mater.* **2009**, *2*, 65–72. [CrossRef]
41. Chow, M.J.; Mondonedo, J.R.; Johnson, V.M.; Zhang, Y. Progressive structural and biomechanical changes in elastin degraded aorta. *Biomech. Model. Mechanobiol.* **2013**, *12*, 361–372. [CrossRef]
42. Lane, B.A.; Cardoza, R.J.; Lessner, S.M.; Vyavahare, N.R.; Sutton, M.A.; Eberth, J.F. Full-field strain mapping of healthy and pathological mouse aortas using stereo digital image correlation. *J. Mech. Behav. Biomed. Mater.* **2023**, *141*, 105745. [CrossRef] [PubMed]
43. Miskolczi, L.; Guterman, L.R.; Flaherty, J.D.; Szikora, I.; Hopkins, L.N. Rapid saccular aneurysm induction by elastase application in vitro. *Neurosurgery* **1997**, *41*, 220–228; discussion 228–229. [CrossRef] [PubMed]
44. Patelis, N.; Moris, D.; Schizas, D.; Damaskos, C.; Perrea, D.; Bakoyiannis, C.; Liakakos, T.; Georgopoulos, S. Animal models in the research of abdominal aortic aneurysms development. *Physiol. Res.* **2017**, *66*, 899–915. [CrossRef] [PubMed]
45. Daugherty, A.; Cassis, L.A. Mouse models of abdominal aortic aneurysms. *Arter. Thromb. Vasc. Biol.* **2004**, *24*, 429–434. [CrossRef]
46. Tornifoglio, B.; Stone, A.J.; Johnston, R.D.; Shahid, S.S.; Kerskens, C.; Lally, C. Diffusion tensor imaging and arterial tissue: Establishing the influence of arterial tissue microstructure on fractional anisotropy, mean diffusivity and tractography. *Sci. Rep.* **2020**, *10*, 20718. [CrossRef]
47. Schneider, C.A.; Rasband, W.S.; Eliceiri, K.W. NIH Image to ImageJ: 25 years of image analysis. *Nat. Methods* **2012**, *9*, 671–675. [CrossRef]
48. Macrae, R.A.; Miller, K.; Doyle, B.J. Methods in Mechanical Testing of Arterial Tissue: A Review. *Strain* **2016**, *52*, 380–399. [CrossRef]
49. Campbell, E.M.; Cahill, P.A.; Lally, C. Investigation of a small-diameter decellularised artery as a potential scaffold for vascular tissue engineering; biomechanical evaluation and preliminary cell seeding. *J. Mech. Behav. Biomed. Mater.* **2012**, *14*, 130–142. [CrossRef]
50. Kim, J.; Baek, S. Circumferential variations of mechanical behavior of the porcine thoracic aorta during the inflation test. *J. Biomech.* **2011**, *44*, 1941–1947. [CrossRef]
51. Horný, L.; Žitný, R.; Chlup, H.; Hana, M. Identification of the material parameters of an aortic wall. *Bull. Appl. Mech.* **2007**, *2*, 173–181.

52. Ruifrok, A.C.; Johnston, D.A. Quantification of histochemical staining by color deconvolution. *Anal. Quant. Cytol. Histol.* **2001**, *23*, 291–299. [PubMed]
53. Fonck, E.; Prod'hom, G.; Roy, S.; Augsburger, L.; Rüfenacht, D.A.; Stergiopulos, N. Effect of elastin degradation on carotid wall mechanics as assessed by a constituent-based biomechanical model. *Am. J. Physiol. Heart Circ. Physiol.* **2007**, *292*, H2754–H2763. [CrossRef]
54. Cox, R.H. Passive mechanics and connective tissue composition of canine arteries. *Am. J. Physiol.* **1978**, *234*, H533–H541. [CrossRef] [PubMed]
55. Wang, R.; Brewster, L.P.; Gleason, R.L. In-situ characterization of the uncrimping process of arterial collagen fibers using two-photon confocal microscopy and digital image correlation. *J. Biomech.* **2013**, *46*, 2726–2729. [CrossRef] [PubMed]
56. Avanzini, A.; Battini, D.; Bagozzi, L.; Bisleri, G. Biomechanical evaluation of ascending aortic aneurysms. *BioMed Res. Int.* **2014**, *2014*, 820385. [CrossRef]
57. Vorp, D.A.; Schiro, B.J.; Ehrlich, M.P.; Juvonen, T.S.; Ergin, M.A.; Griffith, B.P. Effect of aneurysm on the tensile strength and biomechanical behavior of the ascending thoracic aorta. *Ann. Thorac. Surg.* **2003**, *75*, 1210–1214. [CrossRef] [PubMed]
58. Bossone, E.; Eagle, K.A. Epidemiology and management of aortic disease: Aortic aneurysms and acute aortic syndromes. *Nat. Rev. Cardiol.* **2021**, *18*, 331–348. [CrossRef]
59. Isselbacher, E.M. Thoracic and Abdominal Aortic Aneurysms. *Circulation* **2005**, *111*, 816–828. [CrossRef]
60. Zeinali-Davarani, S.; Chow, M.-J.; Turcotte, R.; Zhang, Y. Characterization of Biaxial Mechanical Behavior of Porcine Aorta under Gradual Elastin Degradation. *Ann. Biomed. Eng.* **2013**, *41*, 1528–1538. [CrossRef]
61. Measuring Areas. Read the Docs—QuPath 2.3 Documentation 2021. Available online: https://qupath.readthedocs.io/en/0.2/docs/tutorials/measuring_areas.html (accessed on 25 April 2023).
62. Yousef, S.; Matsumoto, N.; Dabe, I.; Mori, M.; Landry, A.B.; Lee, S.-R.; Kawamura, Y.; Yang, C.; Li, G.; Assi, R.; et al. Quantitative not qualitative histology differentiates aneurysmal from nondilated ascending aortas and reveals a net gain of medial components. *Sci. Rep.* **2021**, *11*, 13185. [CrossRef]
63. Mahutga, R.R.; Schoephoerster, C.T.; Barocas, V.H. The Ring-Pull Assay for Mechanical Properties of Fibrous Soft Tissues—An Analysis of the Uniaxial Approximation and a Correction for Nonlinear Thick-Walled Tissues. *Exp. Mech.* **2021**, *61*, 53–66. [CrossRef] [PubMed]
64. Shazly, T.; Rachev, A.; Lessner, S.; Argraves, W.S.; Ferdous, J.; Zhou, B.; Moreira, A.M.; Sutton, M. On the Uniaxial Ring Test of Tissue Engineered Constructs. *Exp. Mech.* **2015**, *55*, 41–51. [CrossRef]
65. Conti, M. Biomechanical simulations and 3D printing for endovascular device testing. In Proceedings of the Meeting Annuale Centro 3R—GENOVA, Giugno 2019, Genoa, Italy, 20–21 June 2019.

Disclaimer/Publisher's Note: The statements, opinions and data contained in all publications are solely those of the individual author(s) and contributor(s) and not of MDPI and/or the editor(s). MDPI and/or the editor(s) disclaim responsibility for any injury to people or property resulting from any ideas, methods, instructions or products referred to in the content.